Structural Engineering and Mechanics, Vol. 38, No. 6 (2011) 803-823
DOI: http://dx.doi.org/10.12989/sem.2011.38.6.803

Parallel computation for debonding process of externally FRP plated concrete

Tao Xu*[1,2], Yongbin Zhang[3a], Z.Z. Liang[3b], Chun-an Tang[3c] and Jian Zhao[4d]

[1]*Center for Material Failure Modeling Research, Dalian University, Dalian 116622, China*
[2]*State Key Laboratory of Geo-hazard Prevention and Geo-environment Protection, Chengdu University of Technology, Chengdu 610059, China*
[3]*School of Civil Engineering, Dalian University of Technology, Dalian 116024, China*
[4]*Ecole Polytechnique Fédérale de Lausanne, Rock Mechanics Laboratory, CH-1015 Lausanne, Switzerland*

(Received February 3, 2010, Accepted March 23, 2011)

Abstract. In this paper, the three dimensional Parallel Realistic Failure Process Analysis (RFPA^{3D}-Parallel) code based on micromechanical model is employed to investigate the bonding behavior in FRP sheet bonded to concrete in single shear test. In the model, the heterogeneity of brittle disordered material at a meso-scale was taken into consideration in order to realistically demonstrate the mechanical characteristics of FRP-to-concrete. Modified Mohr-coulomb strength criterion with tension cut-off, where a stressed element can damage in shear or in tension, was adopted and a stiffness degradation approach was used to simulate the initiation, propagation and growth of microcracks in the model. In addition, a Master-Slave parallel operation control technique was adopted to implement the parallel computation of a large numerical model. Parallel computational results of debonding of FRP-concrete visually reproduce the spatial and temporal debonding failure progression of microcracks in FRP sheet bonded to concrete, which agrees well with the existing testing results in laboratory. The numerical approach in this study provides a useful tool for enhancing our understanding of cracking and debonding failure process and mechanism of FRP-concrete and our ability to predict mechanical performance and reliability of these FRP sheet bonded to concrete structures.

Keywords: FRP sheet; concrete; debonding; damage; failure process; parallel computation

1. Introduction

The use of fiber reinforced polymers or plastic (FRP) has generated considerable interest for retrofitting existing structures due to its light weight and flexibility, high tensile strength and stiffness and excellent resistance to corrosion and chemicals. In typical strengthening applications, FRP composite sheets are bonded to the tension side of the concrete beam to act as external reinforcement. The FRP composite sheets contribute tensile forces to the internal moment resistance,

*Corresponding author, Associate Professor, E-mail: neuxutao@126.com
[a]Lecturer, E-mail: zybneu@126.com
[b]Associate Professor, E-mail: z.z.liang@163.com
[c]Professor, E-mail: catang@mechsoft.cn
[d]Professor, E-mail: jian.zhao@epfl.ch

which results in an increased load carrying capacity of the concrete beam. The stress transfer from concrete to the FRP composite sheet through the bond generates tensile stresses in the FRP. Thus, the bond between the FRP composite sheet and the concrete plays a critical role in this strengthening method, which controls the efficacy of the repair by providing effective stress transfer from the existing structures to externally bonded FRP plates or sheets and keeping integrity and durability of the composite performance of FRP-concrete hybrid structures. Debonding along the FRP-concrete interface can lead to premature failure of the structure. In order to safely and efficiently take advantage of the strengthening technique, some testing methods have been performed to study the bond property and interfacial behavior of FRP-to-concrete. One of the common testing methods is single shear test in which an FRP sheet or plate is bonded to a concrete prism or block and is subject to tension.

A number of researchers have conducted experimental, analytical investigations on the bond behavior between the FRP composite sheet and the concrete in a single shear test (Aiello and Leone 2008, Bizindavyi and Neale 1999, Bizindavyi *et al.* 2003, Carpinteri and Paggi 2010, Chajes *et al*. 1996, Chen and Teng 2001, Lu *et al*. 2005a, Rabinovitch 2008, Saadatmanesh and Ehsani 1991, Saxena *et al*. 2008, Teng *et al*. 2001, Wu *et al*. 2002, Yang *et al*. 2008). Most have shown that the main failure mode of FRP bonded to concrete in shear tests is concrete failure under shear, occurring generally at a few millimeters from the concrete-to-adhesive interface. The debonding failure of FRP-to-concrete is brittle and catastrophic without any precursor. Bizindavyi and Neale (1999) reported results of an experimental and theoretical investigation of composite-to-concrete bonded joints and indicated that it was often difficult to develop the full composite strength capacity because of premature failure due to delamination and peeling-off of the laminate. Teng *et al*. (2001) presented an experimental study on reinforced concrete cantilever slabs bonded with glass fibre-reinforced polymer strips and found the debonding of FRP strips from the slab started near the fixed end and propagated towards the free end, with the final failure mode being either complete debonding or FRP tensile rupture. Mazzotti *et al*. (2008) performed a series of experimental tests and numerical simulations on FRP-concrete delamination of specimens with different bonded lengths and plate widths. Aielloand Leone (2008) carried out debond tests on FRP-concrete specimens to study the factors of affecting interface behavior. Wu (2002) developed two kinds of nonlinear interfacial constitutive laws describing the pre- and post-interfacial microdebonding behavior to solve the nonlinear interfacial stress transfer and fracture propagation problems for different kinds of adhesive joints in FRP/steel-strengthened concrete or steel structures. Lu (2005a) proposed three bond-slip models of FRP-to-concrete bonded joints based on the predictions of a meso-scale finite element model. Yang *et al*. (2008) reported a simplified interfacial stress formulation for the FRP bonded concrete beams subjected to arbitrary loadings. Saxena *et al.* (2008) investigated the applicability of existing models for the prediction of debonding failure in RC beams externally strengthened with FRP. Rabinovitch (2008) presented the analytical models that are based on linear elastic fracture mechanics (LEFM) approach and a cohesive zone modeling approach. Chen and Teng (2001) made a review of anchorage behavior under single/double shear tests and classified the failure modes into five types including: (a) Concrete failure, (b) Plate tensile failure including FRP rupture or steel yielding, (c) Adhesive failure, (d) FRP delamination for FRP-to-concrete joints, (e) Concrete-to-adhesive interfacial failure, and (f) Plate-to-adhesive interfacial failure. Among these failure modes, FRP delamination for FRP-to-concrete joints is the most common failure mode. As mention above, FRP debonding frequently occurred in the concrete a few millimeters beneath the concrete/adhesive interface and the cracking and fracturing mechanisms are

extremely complex, thus it is both very difficult to directly experimentally measure and theoretically analyze the debonding behavior of FRP-to-concrete.

Recently, numerical methods such as Finite Element Method (FEM) and Boundary Element Method (BEM) have been widely used in the study of debonding of FRP-concrete structures. Initially, linear elastic FEM was employed to study the stress distribution in the bond interface. For example, Chen *et al*. (2001) studied the elastic stress distribution in the interface using FEM based on linear elastic analysis. With a further investigation continuing, gradually, more attention shifted to the nonlinear FE analysis of the concrete-to-FRP interface, aimed at the simulation of the entire debonding process. Wong and Vecchio (2003) carried out numerical simulation on debonding as the failure of the interface elements between the FRP and the concrete through the introduction of the interface elements into the model. Lu (2005b) presented a meso-scale finite element model and simulated the entire debonding process in single shear tests of FRP-to-concrete bonded joints by directly modelling the cracking and failure of concrete elements adjacent to the adhesive layer to avoid the use of interface elements. Chen and Teng (2006) presented a 3D finite element analysis on the stress distributions in a typical shear test set-up for FRP-to-concrete. Freddi and Savoia (2008) studied the problem of debonding of FRP plates glued over a concrete element using boundary integral equations and performed numerical simulation on FRP-concrete debonding problems using boundary element method. Lately, Carpinteri and Paggi (2010) analyzed the snap-back instability problem of end-plate debonding of the external reinforcement in strengthened concrete beams.

Currently, parallel computation has gained a population in computational science and engineering with the fast development of computer parallel computation technique (Chen *et al*. 2008, Danielson *et al*. 2008, Zhang *et al*. 2006). In this paper, a parallel finite-element code, RFPA^{3D}-Parallel, is used for analysis of debonding process of FRP sheets bonded concrete structures using micromechanical model. The micromechanical model for brittle disordered material including concrete and FRP sheet incorporated in RFPA^{3D}-Parallel code is described and the parallel computation method in the model is also briefly introduced. The progressive debonding process of FRP-concrete, the stress transfer evolution along the FRP composite sheet and the failed elements distribution in the FRP-concrete are realistically visualized through parallel computation. Finally, the debonding mechanism of FRP-concrete is also analyzed.

2. Brief outline of RFPA^{3D}-Parallel model

The three dimensional Parallel Realistic Failure Process Analysis (RFPA^{3D}-Parallel) code based on RFPA^{3D} model (Tang *et al*. 2008, Tang *et al*. 2006, Xu *et al*. 2006) is developed for describing and predicting the deformation and fracturing of 3-D brittle disordered materials by considering the heterogeneity of materials. In RFPA^{3D}-Parallel, the model is numerically divided into regular cubic elements. Each cubic element has 8 nodes with three degrees of freedom per node. The heterogeneity of the material is taken into account by assigning different properties to the individual elements according to the real material structure. Modified Mohr-coulomb strength criterion with tension cut-off (Brady and Brown 2004, Jeager *et al*. 2007) was adopted in the model, where a stressed element can damage in shear or in tension. A stiffness degradation approach that a micro-fracturing occurs when the stress of an element satisfies a strength criterion was employed. The degradation of the material properties after element failure was introduced in the model to simulate

strain-softening and discontinuum mechanics problems in a continuum mechanics mode. And a Master-Slave operation control technique was adopted to improve and implement the parallel computation of a large numerical model. In addition, the failed elements were recorded in the model to simulate acoustic emission or seismicities associated with the progressive fracture process.

2.1 Assignment of material properties

In order to reflect the heterogeneity of brittle disordered materials at a meso-level, the mechanical parameters including strength and Young's modulus of the mesoscopic material elements, which are assumed as homogeneous and isotropic, are assumed to follow the Weibull distribution (Weibull 1951) as defined in the following statistical probability density function

$$f(u) = \frac{m}{u_0}\left(\frac{u}{u_0}\right)^{m-1} \exp\left[-\left(\frac{u}{u_0}\right)^{m}\right] \tag{1}$$

where u is the scale parameter of individual element such as strength or Young's modulus and the scale parameter u_0 is related to the average of element parameter, the shape parameter m reflects the degree of material homogeneity and is defined a homogeneity index. According to the Weibull distribution and the definition of homogeneity index, a larger m implies that more elements with the mechanical properties approximated to the mean value and a more homogeneous disordered media. Fig. 1 is the histogram of strength of elements in two numerical specimens that are all composed of one million (100 × 100 × 100) cubic elements with the same size, produced randomly by computer according to the Weibull distribution with the same strength scale parameter 100 but different homogeneity indices 2 and 10. Therefore, the higher value of homogeneity index leads to more homogeneous numerical specimens. In previous paper (Tang *et al*. 2000, Tang *et al*. 2007, Zhu *et al*. 2004), how the homogeneity index affects the macroscopic mechanical response of numerical specimens has been discussed and it is found that the homogeneity index is an important parameter of Weibull distribution to control the macroscopic response of numerical specimen. In this investigation, it is assumed that Young's modulus and strength conform to two independent distributions with the same heterogeneity index (Liang 2005).

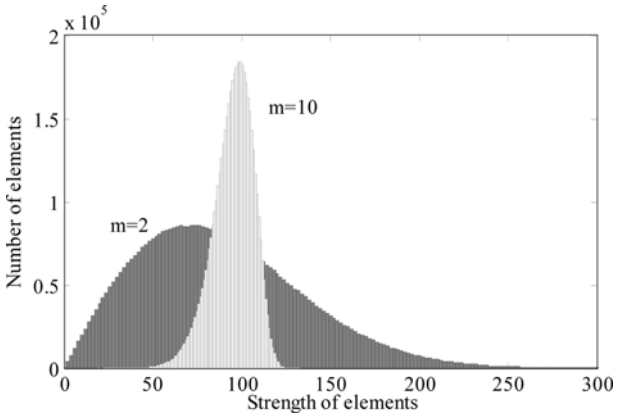

Fig. 1 Histogram of strength of elements in numerical specimen with different homogeneity index (The numerical specimen is shown in Fig. 1, which is composed of 1,000,000 elements and the scale parameter u_0 is 100 MPa)

It needs to be pointed that, as the element sizes used for the plain concrete prism in the present numerical model are much smaller than the maximum aggregate size, a true meso-mechanical model requires the modeling of the meso-level internal structure of concrete, with the difference between the cement mortar and aggregate explicitly considered. The present model is, however, not intended as such a meso-mechanical model. Instead, the present model, referred to as the meso-scale model, aims to use small elements to accurately track the development and propagation of cracks; the elements are still intended to represent the average performance of concrete. Hence, the effect of microstructure such as aggregates, cement mortar and pores in the concrete is homogenized in the model.

2.2 Damage constitutive law

As we know, the FRP sheets in reinforced concrete structures are normally used to carry tensile stresses. The stress-strain laws of the FRP sheets (glass fibre or carbon fibre reinforced plastic ones) used in civil engineering are almost linearly elastic up to its ultimate strength (Ali-Ahmad 2006). Thus, in the paper, the FRP composites and plain concrete are both considered as brittle disordered materials and are analyzed at meso level, and their stress-strain relationship can be described with an elastic damage constitutive law. Compared to plain concrete, FRP composite sheet has much higher strength, relative low elastic modulus and extremely low residual strength. The model is numerically divided into regular cubic elements and the elements are considered to be elastic and its elastic properties can be defined by Young's modulus and Poisson's ratio. The stress-strain curve of the element is considered linear elastic till the given damage threshold is attained, and then is followed by softening. For simplicity, an elastic damage model with constant residual strength is used. The modified Mohr-Coulomb criterion with tension cut-off is used as damage threshold so that the failure of the elements may be either in shear or in tension.

In elastic damage mechanics, the elastic modulus of element may degrade gradually as damage progresses. The elastic modulus of damaged material is defined as follows.

$$E = (1 - D)E_0 \tag{2}$$

where D represents the damage variable. E and E_0 are elastic modulus of the damaged and the undamaged material, respectively. Here the element as well as its damage is assumed isotropic elastic, so the E, E_0 and D are all scalar.

When the mesoscopic element is under uniaxial tensile stress, the constitutive relationship that is elasto-brittle damage with given specific residual strength is shown in Fig. 2. Herein tensile stress shall be referred to as positive and compressive stress as negative for sign convention. No initial damage is incorporated in this model, at the beginning the stress-strain curve is linear elastic and no damage occurs, i.e., $D = 0$. When the maximum tensile stress is reached and beyond the strength of the element, the damage of element occurs. This kind of damage can be called tensile damage.

According to the constitutive relationship of mesoscopic element under uniaxial tension as shown in Fig. 2, the damage evolution of element D can be expressed as

$$D = \begin{cases} 0 & \varepsilon < \varepsilon_{t0} \\ 1 - \dfrac{f_{tr}}{\varepsilon E_0} & \varepsilon_{t0} \le \varepsilon < \varepsilon_{tu} \\ 1 & \varepsilon \ge \varepsilon_{tu} \end{cases} \tag{3}$$

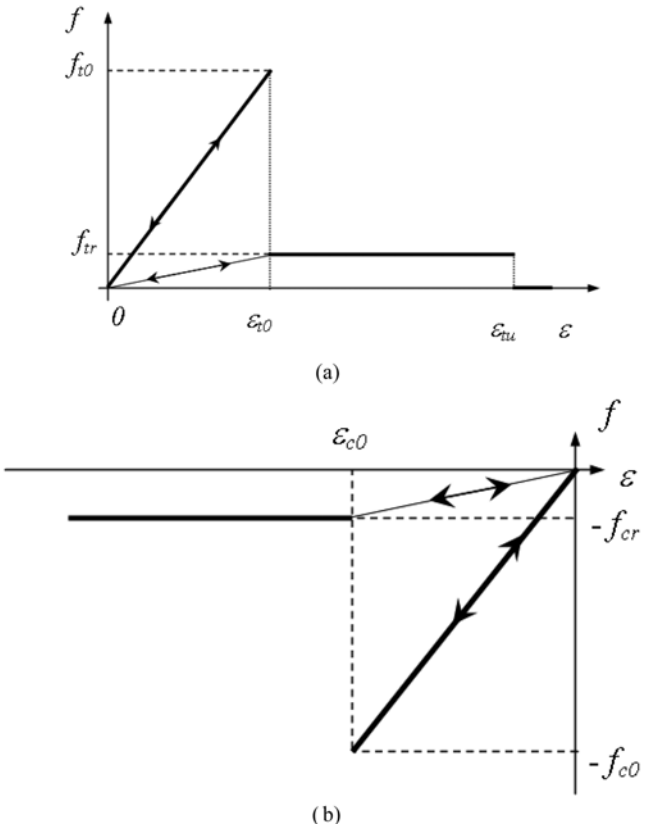

Fig. 2 Elastic damage constitutive law of element under uniaxial (a) tensile stress, and (b) compressive stress

where f_{tr} is the residual uniaxial tensile strength and $f_{tr} = \lambda f_{t0}$ in which λ is the residual strength coefficient and f_{t0} is the uniaxial tensile strength at the elastic limit strain (threshold strain) ε_{t0}. ε_{tu} is the ultimate tensile strain of the element, which indicates that the element would be completely damaged when the tensile strain of element attains this ultimate tensile strain. The ultimate tensile strain is defined as $\varepsilon_{tu} = \eta\varepsilon_{t0}$, in which η is called ultimate strain coefficient.

It is assumed that the damage of mesoscopic element in multiaxial stress field is also isotropic elastic, and therefore the above-described constitutive law for uniaxial tensile stress can be extended to three-dimensional stress states. Under multiaxial stress states the element still damages in tensile mode when the equivalent strain $\bar{\varepsilon}$ (Lemaitre and Desmorat 2005) of the combination of major tensile strain attains the aforementioned threshold strain ε_{t0}. The constitutive law of element subjected to multiaxial stresses can be easily obtained only by substituting the strain ε in Eq. (3) with equivalent strain $\bar{\varepsilon}$.

$$D = \begin{cases} 0 & \bar{\varepsilon} < \varepsilon_{t0} \\ 1 - \dfrac{f_{tr}}{\bar{\varepsilon} E_0} & \varepsilon_{t0} \le \bar{\varepsilon} < \varepsilon_{tu} \\ 1 & \bar{\varepsilon} \ge \varepsilon_{tu} \end{cases} \tag{4}$$

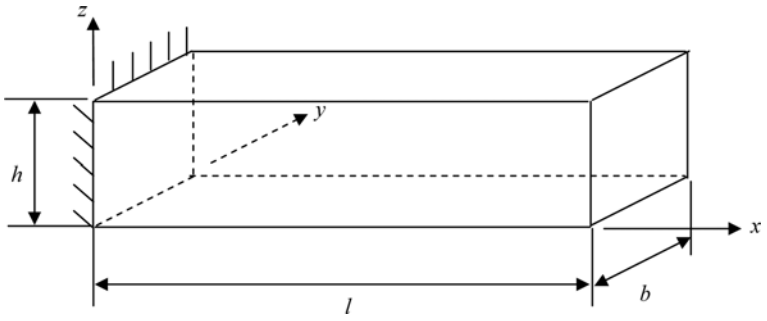

Fig. 3 Scketch of a beam under uniform uniaxial tension

where the equivalent strain $\bar{\varepsilon} = \sqrt{<\varepsilon_1>^2 + <\varepsilon_2>^2 + <\varepsilon_3>^2}$ in which ε_1, ε_2 and ε_3 are the three principal strains, $<>$ stands for the positive part of a scalar and $<x> = (x + |x|)/2$.

Mohr-Coulomb criterion as expressed follows is used as the damage threshold for the damage of elements subjected to compressive and shear stress.

$$F = \frac{1+\sin\phi}{1-\sin\phi}\sigma_1 - \sigma_3 \geq f_{c0} \tag{5}$$

where σ_1 and σ_3 are major and minor principal stress respectively, f_{c0} is uniaxial compressive strength and ϕ is the internal friction angle. It needs to be pointed that the value of σ_3 and σ_1 respectively indicate the magnitude of maximum and minimum compressive stress when these two principal stresses are both compressive since compressive stresses are negative and tensile stresses are positive. This kind of damage is referred to as shear damage.

A similar constitutive law to the tensile is given in Fig. 3 when the element is under uniaxial compression and damaged in shear mode according to the Mohr-Coulomb criterion. The damage variable D can be described as follows.

$$D = \begin{cases} 0 & \varepsilon > \varepsilon_{c0} \\ 1 - \dfrac{f_{cr}}{\varepsilon E_0} & \varepsilon \leq \varepsilon_{c0} \end{cases} \tag{6}$$

where f_{cr} is residual uniaxial compressive strength and is defined as $f_{cr} = \lambda f_{c0}$. In the model, it is assumed that $f_{cr}/f_{c0} = f_{tr}/f_{t0} = \lambda$ hold true when the mesoscopic element is under uniaxial compression or tension.

When the element is under multi-axial stress state and satisfies the Mohr-Coulomb criterion, the shear damage occurs, and the effect of other principal stress in this model during damage evolution process is considered. When the Mohr-Coulomb criterion is met, the minor principal strain (maximum compressive principal strain) ε_{c0} at the peak value of minor principal stress is calculated.

$$\varepsilon_{c0} = \frac{1}{E_0}\left[-f_{c0} + \frac{1+\sin\phi}{1-\sin\phi}\sigma_1 - \mu(\sigma_1 + \sigma_2)\right] \tag{7}$$

In addition, it is assumed that the damage evolution is only related to the maximum compressive principal strain ε_3. Therefore, the maximum compressive principal strain ε_3 of damaged element is used to substitute the uniaxial compressive strain ε in Eq. (6). Thus, the former Eq. (6) can be

extended to biaxial or triaxial stress states.

$$D = \begin{cases} 0 & \bar{\varepsilon} > \varepsilon_{c0} \\ 1 - \dfrac{f_{cr}}{\bar{\varepsilon} E_0} & \bar{\varepsilon} \le \varepsilon_{c0} \end{cases} \tag{8}$$

From the above derivation of damage variable D, which is generally called the damage evolution law in damage mechanics, as well as Eq. (2), the damaged elastic modulus of element at different stress or strain levels can be calculated. The unloaded element keeps its original elastic modulus and strength. That is to say, the element will unload elastically and no residual deformation is incorporated in the numerical model. It must be emphasized that when D = 1, it can be calculated from Eq. (2) that the damaged elastic modulus is zero, which would make the system of equations ill-posed, therefore, in this model a relatively small number, i.e., 1.0e-05 by default is specified to the elastic modulus under this condition. At any event, the damage of elements in tension is preferential to that in shear.

As we know, acoustic emission (AE), accompanied by crack opening, is predominantly related to the release of elastic energy within the bulk of the brittle disordered materials. One method of detecting microcracking during brittle material deformation experiments is by monitoring the acoustic emission (AE) or microseismic events produced during deformation to detect the onset and the evolution of stress-induced cracks and analyze the spatial and temporal rogression of microcracks (Carpinteri *et al*. 2007, Grosse and Finck 2006). Locker (Lockner 1993, Lockner *et al*. 1991) has analyzed catalogues of AE events recorded during loading tests in rock in terms of the information they give about the accumulated state of damage in a material. And combine this measured damage state with a model for the weakening behavior of cracked solids, which shows that reasonable predictions of the mechanical behavior are possible. Based on this background knowledge, as an approximation, it is reasonable to assume that the AE counts are proportional to the number of damaged elements and the strain energies released by damaged elements are all in form of acoustic emissions (Tang 1997). In this model, a single AE event represents a micro-crack forming event to indirectly assess the damage evolution, and the AE energy release is related to the strain energy of element before and after its damage. Therefore, the AE counts are accounted by the number of damaged elements and the energy releases are calculated from the strain energy release of damaged elements. Based on this assumption, the cumulative AE counts and cumulative AE energy release can be realistically simulated with above-mentioned numerical model. In the model, by recording the counts of failed elements, the acoustic emission or microseismicities associated with the progressive failure can be simulated in the model that allows elements to fail when overstressed.

2.3 Implementation of parallel computation

The parallel procedure consists of a parallel preprocessing phase mainly consisting of portioning and parallel setup, a parallel analysis phase that includes explicit message passing among each partition on separate processors, and a parallel postprocessing phase to gather separate parallel output data into a single coherent database file. For effective parallel computing, it is critical to balance the computational load among processors while minimizing interprocessor communication. Thus, a suitable partition to the meshed model needs to be made before performing parallel

analysis. The partitioning is made to create partitions of nearly equal element computational effort and to minimize the number of partition interfaces with regard to the element calculations, since it involves more computational effort than the lumped mass equation solving. The number of partition interface nodes directly affects the amount of interprocessor communication, since it results in nodes that are shared by processors. The parallel finite element program in this paper mainly includes five parts: finite element mesh generation; finite element mesh data partition; calculation of subdomain stiffness matrix and load and the formation of the system equations; iterative solution of system equations; solution of subdomain nodal displacement and stress. Only the first part of the finite element mesh generation is in serial operation, other four parts are in parallel operation. The parallel analysis is achieved by the parallel FEM module incorporated into RFPA^{3D}-Parallel code, which is developed with MPI (Message-Passing Interface) on the Linux Redhat9.0 platform by using FORTRAN90 language and C++ language. MPI is a standard specification for message-passing libraries, and it also provides a programming environment to develop parallel computer code. A Master-Slave parallel operation control technique is adopted for data distribution and communication in the FEM analysis module in RFPA^{3D}-Parallel code. Firstly the data prepared in the parallel pre-processing phase are sent to the console node which serves as a master node, and the sub-domains partitioned in parallel preprocessing phase are distributed to many computer nodes (processors) which serve as the slaves by using an algorithm termed Domain Decomposition Method (DDM). Each slave (processor) performs an analysis on its own assigned sub-domain by an independent FEM program. The processors calculating the sub-domains can exchange information between each other and the total disequilibrium force is calculated. The iterative calculation will continue until the total disequilibrium force reaches to a give small value. The calculated results will be returned back to the master node if all slave nodes have finished their tasks. These partitioned sub-domains are performed as if they were separate analyses, except that contributions to the force vectors are sent to and from other processors for the shared nodes. An effective resolver for large-scale linear functions may save much time in the parallel computing process. In the FEM module, PCG (Preconditioning Conjugate Gradient) method is used to improve iteration performance greatly in resolving the linear systems of equations. The parallel computation was carried out on Lenovo Shenteng 1800 parallel computer cluster. The cluster had 32 nodes and 64 processors, and the memory was 2G in each node.

3. Verification of RFPA^{3D}-Parallel model

n this section, the RFPA^{3D}-Parallel model is validated by comparisons between simulated results by RFPA^{3D}-Parallel, Ansys, Jiang and Zhang (1990) and theoretical result for a beam under uniform uniaxial tension. Meanwhile, the run time consumed in five parts during parallel computation is analyzed. The same model and mechanical parameters are selected from Jiang and Zhang (1990). The beam geometry is shown in Fig. 3. The length l, the height h and the thickness b of the cantilever, are 100 millimeters, 20 millimeters and 10 millimeters, respectively. The elastic modulus and the possion's ratio are 150 GPa and 0.25, respectively. The uniform tensile stress acted on the right end of the cantilever is 200 MPa.

For the finite element modeling, the model is divided into $100 \times 20 \times 10$ (20000) cubic elements with 23,331 nodes and 69,993 degrees of freedom in total. Two computing nodes and four calculating processes were adopted to carry out the computation. In contrast, the computation on the

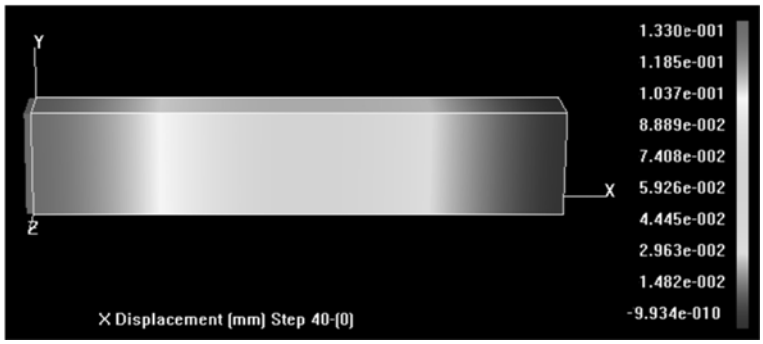

Fig. 4 Simulated deformation distribution along the beam under uniform tension

Table 1 Comparison between computational results and theoretical result of displacement in x direction for a beam under uniform tension

	RFPA^{3D}-Pallel (20000 elements)	Ansys (20000 elements)	Jiang and Zhang (5 elements)	Theoretical result
Deformation (cm)	13.33	13.292	13.18	13.333
Relative Error	0.0225%	0.310%	1.1%	-

model with the same configuration by Ansys was also performed. The theoretical solution to the displacement in the x direction for a homogeneous beam under uniaxial tensile stress aced on x face is

$$u = \frac{Pl}{E} \tag{9}$$

Fig. 4 shows the simulated deformation distribution along the beam under uniform tension. It can be seen from Fig. 4 that the beam deformation in x direction is 0.133m. Table 1 shows the ultimate displacement in the x direction obtained from those computations with RFPA^{3D}-Parallel, Ansys, Jiang and Zhang and theoretical solution as described in Eq. (9). The theoretical solution for the deformation of the beam in x direction is 13.333 cm. The simulated displacements by RFPA^{3D}-Parallel, Ansys, Jiang and Zhang are 13.33 cm, 13.292 cm and 13.18 cm, repectively. The relative error between RFPA^{3D}-Parallel and theoretical solution is 0.0225%, whereas the relative errors among Ansys, Jiang and Zhang and theoretical solution are 0.310% and 1.1%, respectively. Compared with the simulated results by Ansys and Jiang and Zhang, the calculated result by RFPA^{3D}-Parallel code is much closer to the theoretical solution. It illustrates that RFPA^{3D}-Parallel code employed in this paper is reliable and accurate in performing finite element computation on FRP-concrete.

The run time consumed in five parts during parallel computation was tracked as shown in Table 2 to analyze the key influencing factor to the whole performance of parallel finite element program. As seen in Table 2, most of the computation time beyond 60% in FEA is spent on solving the system of algebraic equations related to static equilibrium equations and the iterative process is the most frequent phase for data exchange in the FEA. Four global communications and two local communications are required in each iteration step. Data traffic increases with the number of

Table 2 Run time and proportion of each part for parallel finite element program

Part name	Run time (s)	Proportion
Mesh generation	0.102	1.188%
Data partition	0.078	0.909%
Subdomain stiffness matrix and load	1.654	19.266%
Iterative solution of system equations	5.300	61.736%
Solution of nodal displacement and stress	1.451	16.902%
Run time in total	8.585	100%

equation iterations, which has great impact on the calculation performance. The two parts, calculation of subdomain stiffness and load and the formation of the system equations together with solution of subdomain nodal displacement and stress, are the most time-consumed parts in addition to the part of iterative solution of system equations. The two parts are already highly parallel and will not obviously affect the performance of parallel programs. Since the numerical model with 23,331 nodes and 69,993 degrees of freedom is still relatively small at a scale, the run time consumed on mesh generation and data partition is very short, it account to very small proportion of the whole run time. The run time on mesh generation will become long with the increase of the model scale since it is in serial operation, whereas the run time on several other parts especially solution of system equations will correspondingly increase in the proportion of time due to the increase in model size. In addition, details about the speedups and efficiency of parallel performance evaluation on RFPA^{3D}-Parallel code can be referred to Zhang (2007).

4. Numerical model

Fig. 5 shows a typical configuration for a single shear test of FRP sheet bonded to concrete. Left, right and bottom sides of the specimen are constrained in order to have no displacements in the direction normal to the surface and free displacements tangent to it. The numerical model has a geometry of 150 mm × 50 mm × 100 mm in this study. The specimen has been discretized into a 150 × 50 × 100 (750,000 cubic elements) mesh. The plain concrete block of nominal dimensions,

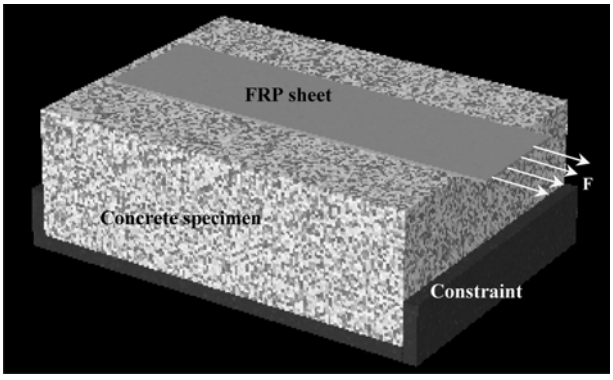

Fig. 5 Numerical model for single shear test on FRP sheet bonded to concrete

length (120 mm), width (100 mm), and height (45 mm) was used. The external FRP sheet with a dimension of 40 mm in width, and 120 mm in length and 1mm in thickness is bonded on the middle upper surface of the plain concrete block. The concrete block was place in the fixture and load was applied to the FRP sheet. The material properties of the plain concrete are as follows: Uniaxial compressive strength, $f_c = 36$ MPa, Elastic Modulus, $E = 20$ GPa and the ratio of uniaxial compressive strength to uniaxial tensile strength is 10. The modulus of elasticity and ultimate tensile strength of the reinforced FRP sheet in the primary direction of E-glass fiber is taken as 30 GPa and 640 MPa, respectively (Xiao *et al*. 2004).

In this study, a perfect bond between FRP sheet and the concrete is assumed, viz., the use of interface elements is avoided, instead, debonding is directly simulated by modelling the cracking and failure of concrete elements adjacent to the FRP sheet. The advantage of this approach is that the debonding behaviour can be predicted and the process and mechanism of debonding can be better investigated using an appropriate constitutive model for concrete, without recourse to an interfacial bond-lip model. The approach also provides a useful way for understanding the debonding failure process and mechanism as only limited experimental observations of the debonding failure process can generally be made due to the microscopic details involved in and the suddenness of a debonding failure. In addition, as described above, we aims to use small elements representing the average performance of concrete to track the development and propagation of cracks, and thus the effect of microstructure such as aggregates, cement mortar and pores in the concrete is averaged in the model.

In the numerical computation, an external tensile displacement at a constant rate of 0.002 mm/step in the x axial direction was applied and the stress as well as the deformation in each element was computed to simulate the complete debonding failure process of the FRP bonded to concrete. It is noted that the displacement loading mode is equivalent to displacement control in the analogous servo-controlled laboratory test, so that the softening branch of the load-displacement crve and the debonding process could be followed. At each step, the stress states in some elements may satisfy the strength criterion. Such elements are damaged and weakened according to the rules specified by the strength criterion. The stress and deformation distribution throughout the specimen are then adjusted instantaneously to reach a new equilibrium state.

5. Modeling results and discussion

The final simulated debonding failure mode of FRP sheet bonded to concrete in single shear was shown in Fig. 6. In Fig. 6, the FRP sheet on the plain concrete specimen was not displayed to facilitate the observation of the debonding failure results of the FRP sheet bonded to concrete. The final failure of the specimen was produced by debonding, resulting in a nearly complete separation of the FRP sheet from the concrete block. Observation of the debonded surface between FRP sheet and concrete block indicated that the failure occurred in a thin interfacial layer at a few millimeters close to the FRP-concrete interface. Compared with the experimental results conducted by other researchers (Ali-Ahmad *et al*. 2006, Mazzotti *et al*. 2008, Yao *et al*. 2005), it can be found that the simulated final debonding failure mode of FRP sheet bonded to concrete in single shear is phenomenologically in agreement with the experimental results. The agreement between numerical simulation and experimental result indicates that the numerical model in this study is suitable to simulate the cracking and debonding failure process of FRP sheet bonded to concrete.

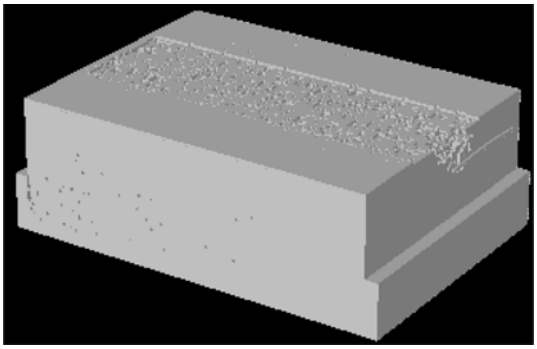

Fig. 6 Numerically simulated failure result of FRP sheet in single shear test

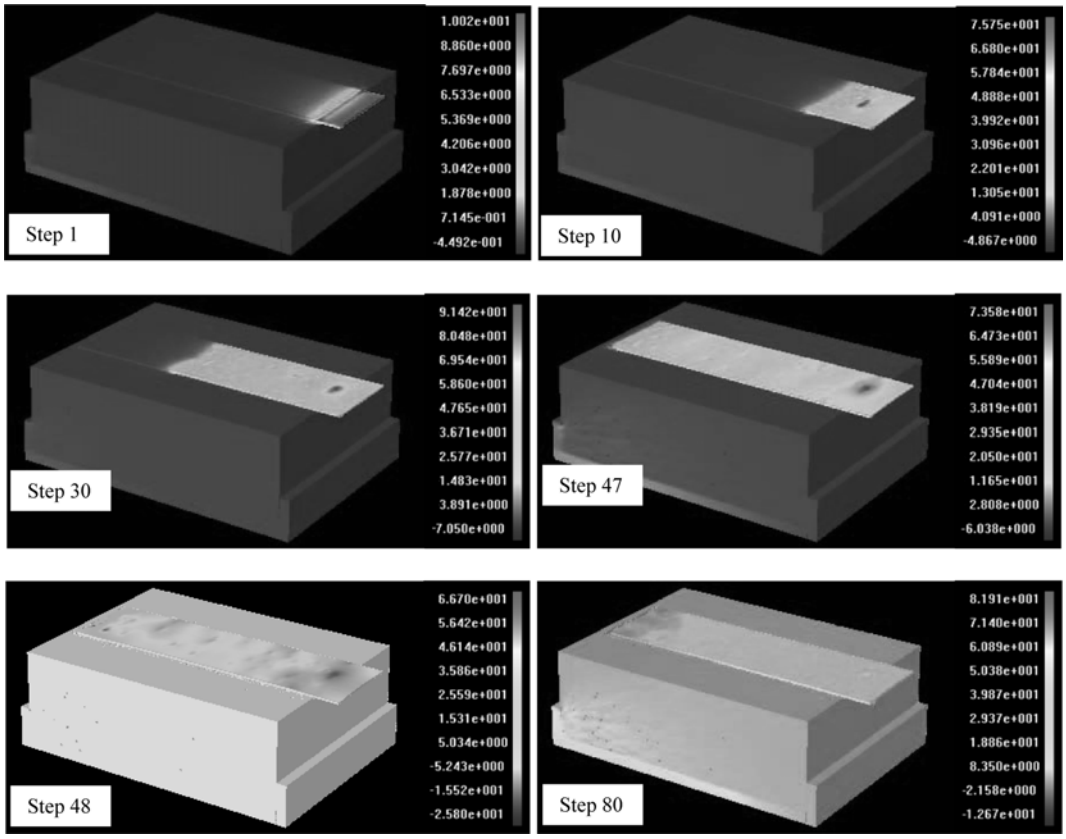

Fig. 7 Numerically simulated tensile stress fields evolution of FRP sheet in single shear test

Fig. 7 and Fig. 8 are the numerically simulated tensile stress fields and displacement deformation field evolution in FRP sheet bonded to concrete under single shear test, respectively. Meanwhile, the simulated debonding process of FRP-concrete interface underneath the FRP sheet by cutting section and failed elements distribution (or analogous to AE) of the FRP-to-concrete in single shear, are respectively presented in Fig. 9 and Fig. 10 to facilitate the observation and evaluation of the onset and evolution of stress induced crack and the spatial and temporal progression of microcracks. It

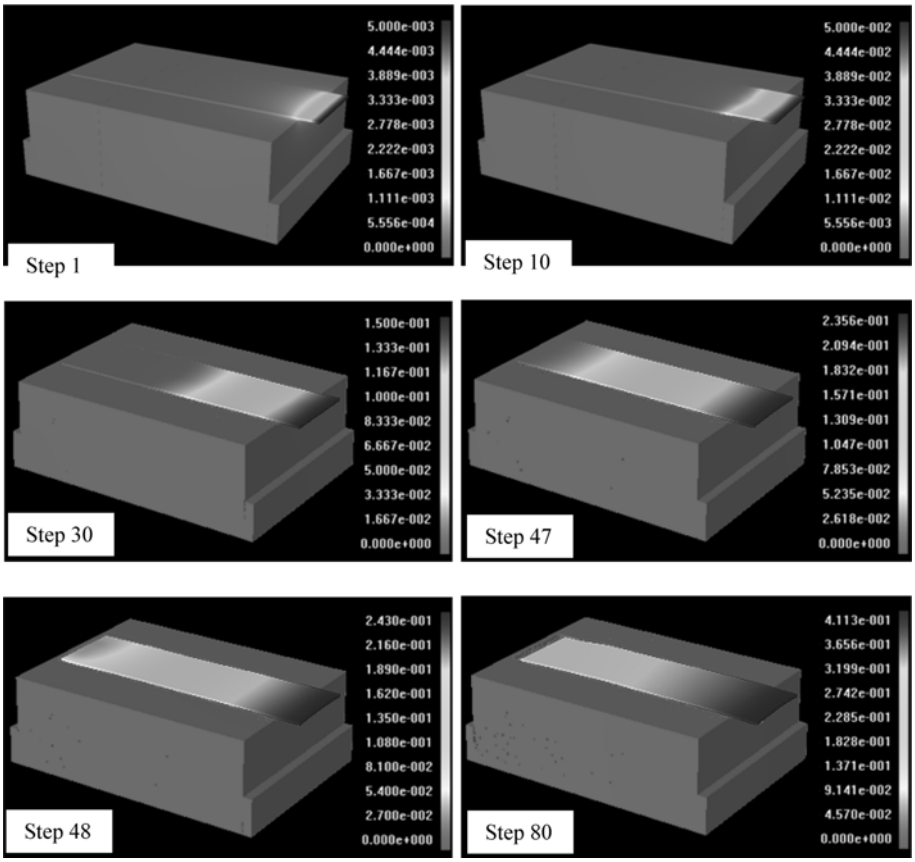

Fig. 8 Numerically simulated deformation fields evolution of FRP sheet in single shear test

noted that the red failed sites indicate the elements failed in tension and the white ones mean the elements failed in shear in Fig. 10 though there were few white failed sites induced by shear. It can be obviously seen from these numerical simulations that in the early stage of loading, significant bond stresses concentrated and developed near the loaded end of FRP sheet in which the distribution of stress and deformation is basically uniform at a macroscopic scale (step 1 in Fig. 7 and Fig. 8) though some weak elements of concrete beneath the FRP sheet damaged and failed in tension (the failed sites indicated by red color) as shown in the step 1 in Fig. 9 and Fig. 10. Meanwhile, it can also be seen that the stress and deformation is approximately zero up to a large distance from the loaded end (step 1 in Fig. 7 and Fig. 8). As the tensile load on FRP sheet increases, there is a rapid increase in deformation on approaching the loaded end, meanwhile, the bond stresses increase, the effective bond zone expands and the tensile stress of FRP transferred inby. The region of high strain gradient appears to be gradually shifted inward along the length of the FRP sheet (step 10 and 30 in Fig. 7 and Fig. 8). More weak concrete elements near the FRP-to-concrete interface damaged and failed under the high tensile stress as can be seen in the step 10 and 30 in Fig. 9 and Fig. 10 that more new red failure sites on plain concrete block beneath the FRP sheet develop and the stress in FRP-to-concrete redistributes and transfers. Further increases in tensile stress lead to a further stress transfer inward along the FRP-to-concrete and a further increase

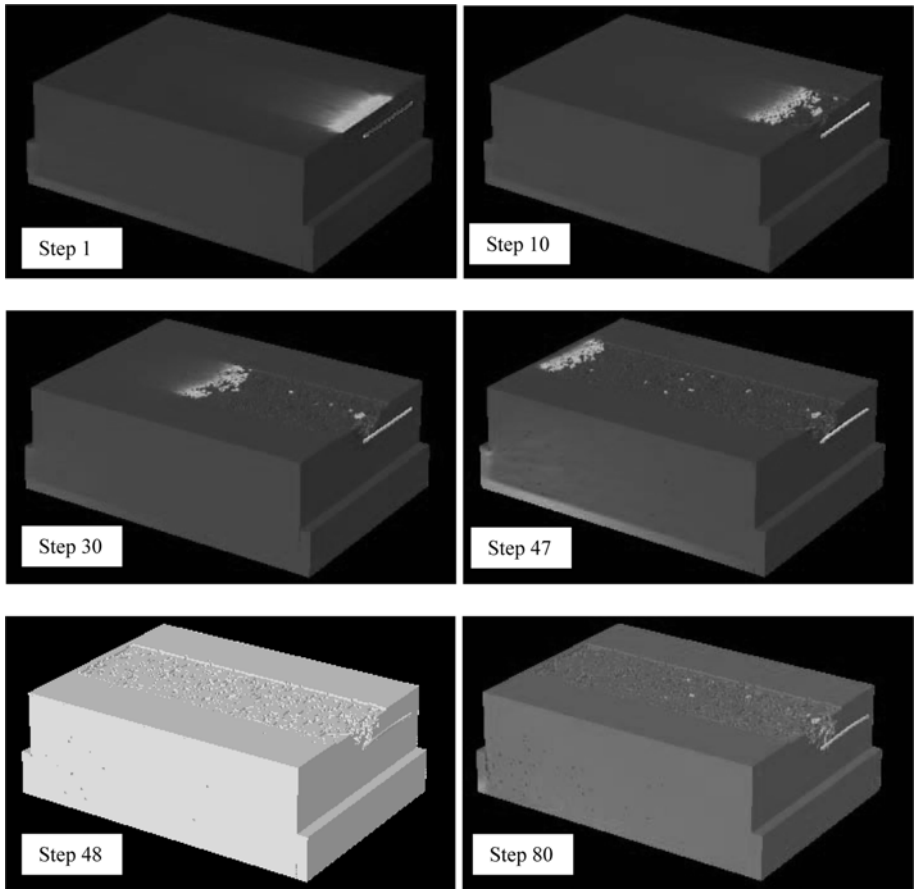

Fig. 9 Numerically simulated concrete cracking and debonding process of FRP-to-concrete

in the elongation and coalescence of the failure sites, which results in a significant increase of failed elements. When the maximum bond stress reaches the local bond strength, clusters of micro-cracking near the interface commences due to the damage of concrete elements (step 47 in Fig. 7, Fig. 8, Fig. 9 and Fig. 10). The bond stresses near the loaded end then decrease, and the effective bond zone continues to expand towards the free end. Finally, when full debonding has been reached, the bond stresses close to the loaded end are very small, indicating the formation of a macro-crack. Finally, the eventual failure of the specimen is symbolized by disintegration of the specimen with the elements failure events sharply decreasing and no obvious element failure events occurrence (at step 48 and step 80 in Fig. 10). This macro-crack corresponds to the surface of the debonded concrete layer observed in a laboratory test. Afterwards, the effective bond zone moves away from the loaded end towards the free end as the macro-crack propagates towards the free end. It is needed to be noticed that there is a significant spatial variation in the axial stress in the FRP sheet, where it is expected to be constant for completely homogeneous material. The fluctuations in the axial stress were found to be due to local material variations in the FRP sheet and concrete caused by material heterogeneity at a meso-scale. Based on the simulated stress and displacement deformation fields evolution along the length FRP sheet, the deformation distribution can thus be

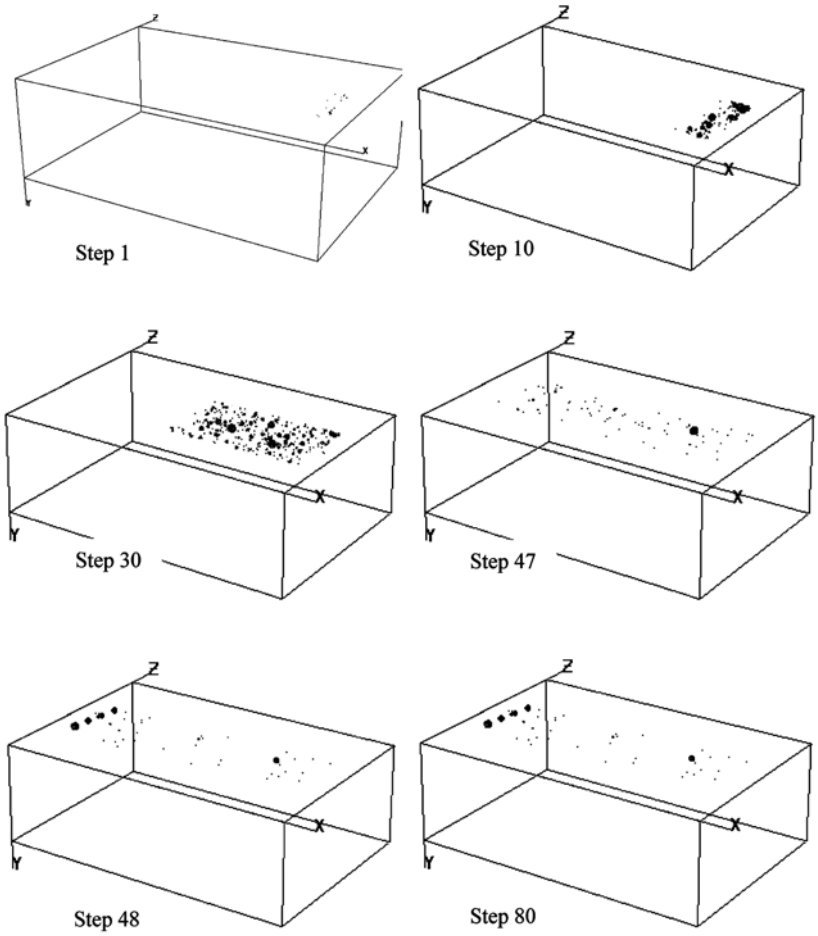

Fig. 10 Numerically simulated failed elements distribution (or AE) in FRP-to-concrete debonding

divided into three main zones: (1) the unstressed zone; (2) the stress transfer zone; and (3) the fully debonded zone. These numerical simulations are phenomenologically in good agreement with the observed results in laboratory (Ali-Ahmad *et al.* 2006). The results indicate that AE events induced by elements failure can be taken as the precursor of macro-fracture of the specimens and acoustic emission is very useful in characterizing the different stages of microstructural damage. The effect of length and width of FRP sheet on bond behavior will be analyzed and discussed in the sequential study.

Fig. 11 shows typical distributions of strains in the FRP sheet. It can be seen that the region of high strain gradient moves further down along the length of the FRP sheet as the global slip increases. At the early stage of loading the FRP strain is minimal beyond a small distance from the loaded end (as shown the step 1 in Figs. 7 and 11), indicating that almost all the applied load is resisted within this small area. With the increase in the applied load, the increase of FRP strain is gradual and the region of high strain gradient appears to be shifted downward. Meanwhile, microcracking emerged gradually on the loaded end part of FRP plate, which leads to an obvious

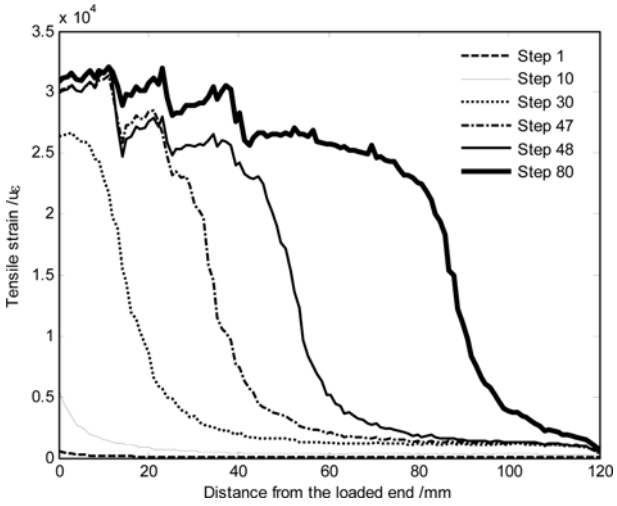

Fig. 11 Simulated strain distribution along FRP sheet

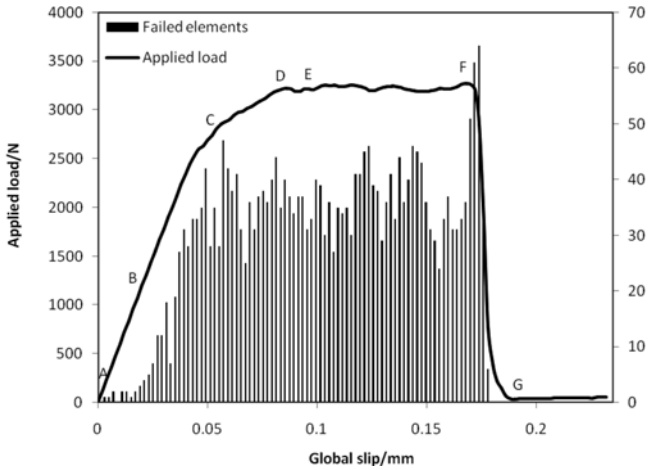

Fig. 12 Numerically simulated load versus global slip response and AE characteristic curve

change of the strain distribution in the FRP strip indicating the propagation of local debonding. The strains in the debonded part of the FRP sheet appear to level off upon crossing the high strain gradient. Strain gradients are typically produced by discontinuities such as a crack. The strain gradient in Fig. 11 is caused by the cracks in the interface close to the free edge of the concrete. The downward shift in the high strain gradient suggests that cracks between concrete and FRP composite initiates in the prepeak portion of the load response. The propagation of debonding is more clearly reflected by the strain distribution as shown in Figs. 7-10, which confirmed that there is progressive crack propagation as the global slip increases. When the ultimate load was reached, the FRP sheet was almost completely debonded. It may be noted that a large part of the FRP sheet near the far end still had minimal strain when the ultimate load was reached, confirming the concept of effective bond length implying that increasing the bond length beyond a certain value does not

further increase the bond strength.

Fig. 12 is the applied load versus global slip response and associated AE characteristic curve, the final debonding failure mode of specimen. The modeling results in Figs. 7-10 correspondingly marked as point A, B, C, D, E and F in the applied load versus global slip response curve. It can be seen from Fig. 12 that the load response versus global slip is initially approximately linear at the early stage which is shown as segment OB. With a continuous increase in the applied load, the test response is nonlinear (segment BD) up to peak load and the load essentially remains constant (segment DF) up to failure. The final failure of the specimen was sudden which is shown as segment FG and produced by debonding, resulting in a complete separation of the FRP sheet from the concrete block. Based on the applied load versus global slip response and the simulated stress evolution along the length FRP sheet, the deformation and debonding process can thus be divided into four stages, i.e., elastic stage (segment OB), elastic-softening stage (segment BD), elastic-softening-debonded stage (segment DF) and softening-debonded stage (segment FG), which is accordance with the analytical analysis (Yuan *et al*. 2004). Moreover, compared with the experimental results such as Fig. 5 in work (Ali-Ahmad *et al*. 2006), it can be found that the simulated final debonding failure mode and applied load versus global slip response of FRP sheet bonded to concrete in single shear are phenomenologically in agreement with the experimental results. The agreement between numerical simulation and experimental result indicates that the numerical model in this study is suitable to simulate the cracking and debonding failure process of FRP sheet bonded to concrete.

6. Conclusions

Generally, it is difficult to thoroughly observe the interfacial debonding failure process of the FRP bonded to concrete in laboratory. In this paper, a micro-mechanical damage model was established and incorporated into the Realistic Failure Process Analysis code, and large-scale parallel computation method for debonding failure analysis of the FRP bonded to concrete block was also implemented. In the model, the heterogeneity of concrete on a meso-scale was taken into consideration in order to realistically demonstrate the mechanical characteristics of concrete. Degradation of small elements is used to simulate the crack propagation in the concrete layer adjacent to FRP. In addition, concrete elements are connected with FRP elements directly without additional interface elements, so the debonding is directly modeled with fracture of concrete elements. Based on the damage model described above, three dimensional debonding failure process for FRP sheets bonded to concrete was performed to investigate the FRP-to-concrete bond behavior. Based on the numerical results presented in this paper, it is founded that the progressive debonding of FRP attached to a concrete substrate is produced by an interfacial crack, which forms and propagates along the interface between the concrete block and the FRP sheet. Based on the simulated stress and displacement deformation fields evolution along the length FRP sheet, the deformation distribution can thus be divided into three main zones: (1) the unstressed zone; (2) the stress transfer zone; and (3) the fully debonded zone. The stress transfer zone advances along the bonded length of FRP as the crack propagates. Once the crack initiates in the interface, it initially grows in a stable manner with increasing stress. Moreover, AE events induced by elements failure accompanied by interfacial cracks growth can be taken as the precursor of macro-fracture of the specimens and acoustic emission is very useful in characterizing the different stages of

microstructural damage. Numerical simulations agreed well with the experimental findings in laboratory and visually reproduce the complete debonding failure process of FRP-concrete. The numerical approach in this study provides a useful tool for understanding the debonding failure process and mechanism as only limited experimental observations of the debonding failure process can generally be made due to the microscopic details involved in and the suddenness of a debonding failure. It is of great help to further understand the cracking and debonding failure process and mechanisms of FRP-to-concrete. With the further research, the effect of length and width of FRP sheet on bond behavior will be analyzed and discussed in the sequential study.

Acknowledgements

The joint financial supports provided by the Sino-Swiss Science and Technology Cooperation Program-The Exchange Program (EG22-032009), the opening fund of State Key Laboratory of Geo-hazard Prevention and Geo-environment Protection, Chengdu University of Technology (SKLGP2010K008), and National Natural Science Foundation of China (grant no. 50809012, 50778046, 50804006 and 51079017) is highly acknowledged.

References

Aiello, M.A. and Leone, M. (2008), "Interface analysis between FRP ebr system and concrete", *Composites Part B-Eng.*, **39**(4), 618-626.

Ali-Ahmad, M., Subramaniam, K. and Ghosn, M. (2006), "Experimental investigation and fracture analysis of debonding between concrete and FRP sheets", *J. Eng. Mech.*, **132**(9), 914-923.

Bizindavyi, L. and Neale, K.W. (1999), "Transfer lengths and bond strengths for composites bonded to concrete", *J. Compos. Constr.*, **3**(4), 153-160.

Bizindavyi, L., Neale, K.W. and Erki, M.A. (2003), "Experimental investigation of bonded fiber reinforced polymer-concrete joints under cyclic loading", *J. Compos. Constr.*, **7**(2), 127-134.

Brady, B.H.G. and Brown, E.T. (2004), *Rock Mechanics for Underground Mining*, Kluwer Academic Publishers, London.

Carpinteri, A., Lacidogna, G. and Paggi, M. (2007), "Acoustic emission monitoring and numerical modeling of FRP delamination in rc beams with non-rectangular cross-section", *Mater. Struct.*, **40**(6), 553-566.

Carpinteri, A. and Paggi, M. (2010), "Analysis of snap-back instability due to end-plate debonding in strengthened beams", *J. Eng. Mech.*, **136**(2), 199-208.

Chajes, M.J., Finch, W.W., Januszka, T.F. and Thomson, T.A. (1996), "Bond and force transfer of composite material plates bonded to concrete", *Aci. Struct. J.*, **93**(2), 208-217.

Chen, H.Q., Ma, H.F., Tu, J., Cheng, G.Q. and Tang, J.Z. (2008), "Parallel computation of seismic analysis of high arch dam", *Earthq. Eng. Eng. Vib.*, **7**(1), 1-11.

Chen, J.F. and Teng, J.G. (2001), "Anchorage strength models for FRP and steel plates bonded to concrete", *J. Struct. Eng.-Asce*, **127**(7), 784-791.

Chen, J.F. and Teng, J.G. (2006), "Special issue on bond behaviour of FRP in structures", *Adv. Struct. Eng.*, **9**(6), 719-719.

Chen, J.F., Yang, Z.J. and Holt, G.D. (2001), "FRP or steel plateto-concrete bonded joints: Effect of test methods on experimental bond strength", *Steel Compos. Struct.*, **1**(2), 231-244.

Danielson, K.T., Akers, S.A., O'Daniel, J.L., Adley, M.D. and Garner, S.B. (2008), "Large-scale parallel computation methodologies for highly nonlinear concrete and soil applications", *J. Comput. Civil Eng.*, **22**(2), 140-146.

Freddi, F. and Savoia, M. (2008), "Analysis of FRP-concrete debonding via boundary integral equations", *Eng.*

Fract. Mech., **75**(6), 1666-1683.
Grosse, C.U. and Finck, F. (2006), "Quantitative evaluation of fracture processes in concrete using signal-based acoustic emission techniques", *Cement Concrete Compos.*, **28**(4), 330-336.
Jeager, J.C., Cook, N.G.W. and Zimmerman, R. (2007), *Fundamentals of Rock Mechanics*, Wiley-Blackwell.
Jiang, J. and Zhang, D. (1990), *Elastoplastic Finite Element Analysis for Structures*, China Astronautic Publishing House, Beijing.
Lemaitre, J. and Desmorat, R. (2005), *Engineering Damage Mechanics*, Springer-Verlag, Berlin.
Liang, Z.Z. (2005), "Three-dimensional failure process analysis of rock and associated numerical test", PhD, Northeastern University of China, Shenyang.
Lockner, D. (1993), "The role of acoustic emission in the study of rock fracture", *Int. J. Rock Mech. Min.,* **30**(7), 883-899.
Lockner, D.A., Byerlee, J.D., Kuksenko, V., Ponomarev, A. and Sidorin, A. (1991), "Quasi-static fault growth and shear fracture energy in granite", *Nature*, **350**(39-42).
Lu, X.Z., Teng, J.G., Ye, L.P. and Jiang, J.J. (2005a), "Bond-slip models for FRP sheets/plates bonded to concrete", *Eng. Struct.*, **27**(6), 920-937.
Lu, X.Z., Ye, L.P., Teng, J.G. and Jiang, J.J. (2005b), "Meso-scale finite element model for FRP sheets/plates bonded to concrete", *Eng. Struct.*, **27**(4), 564-575.
Mazzotti, C., Savoia, M. and Ferracuti, B. (2008), "An experimental study on delamination of FRP plates bonded to concrete", *Constr. Build. Mater.*, **22**(7), 1409-1421.
Rabinovitch, O. (2008), "Debonding analysis of fiber-reinforced-polymer strengthened beams: Cohesive zone modeling versus a linear elastic fracture mechanics approach", *Eng. Fract. Mech.*, **75**(10), 2842-2859.
Saadatmanesh, H. and Ehsani, M.R. (1991), "Rc beams strengthened with GFRP plates. 1. Experimental-study", *J. Struct. Eng.-Asce*, **117**(11), 3417-3433.
Saxena, P., Toutanji, H. and Noumowe, A. (2008), "Failure analysis of FRP-strengthened RC beams", *J. Compos. Constr.*, **12**(1), 2-14.
Tang, C.A. (1997), "Numerical simulation of progressive rock failure and associated seismicity", *Int. J. Rock Mech. Min.,* **34**(2), 249-261.
Tang, C.A., Liang, Z.Z., Zhang, Y.B., Chang, X., Tao, X., Wang, D.G., Zhang, J.X., Liu, J.S., Zhu, W.C. and Elsworth, D. (2008), "Fracture spacing in layered materials: A new explanation based on two-dimensional failure process modeling", *Am. J. Sci.*, **308**(1), 49-72.
Tang, C.A., Liu, H., Lee, P.K.K., Tsui, Y. and Tham, L.G. (2000), "Numerical studies of the influence of microstructure on rock failure in uniaxial compression - Part I: Effect of heterogeneity", *Int. J. Rock Mech. Min.,* **37**(4), 555-569.
Tang, C.A., Tham, L.G., Wang, S.H., Liu, H. and Li, W.H. (2007), "A numerical study of the influence of heterogeneity on the strength characterization of rock under uniaxial tension", *Mech. Mater.*, **39**(4), 326-339.
Tang, C.A., Zhang, Y.B., Liang, Z.Z., Xu, T., Tham, L.G., Lindqvist, P.A., Kou, S.Q. and Liu, H.Y. (2006), "Fracture spacing in layered materials and pattern transition from parallel to polygonal fractures", *Phys. Rev. E*, **73**(5), 0561201-0561209.
Teng, J.G., Cao, S.Y. and Lam, L. (2001), "Behaviour of gfrp-strengthened rc cantilever slabs", *Constr. Build Mater.*, **15**(7), 339-349.
Weibull, W. (1951), "A statistical distribution function of wide applicability", *J. Appl. Mech.*, **18**(3), 293-297.
Wong, R.S.Y. and Vecchio, F.J. (2003), "Towards modeling of reinforced concrete members with externally bonded fiber-reinforced polymer composite", *Aci Struct. J.*, **100**(1), 47-55.
Wu, Z., Yuan, H. and Niu, H. (2002), "Stress transfer and fracture propagation in different kinds of adhesive joints", *J. Eng. Mech.*, **128**(5), 562-573.
Xiao, J., Li, J. and Zha, Q. (2004), "Experimental study on bond behavior between FRP and concrete", *Constr. Build Mater.*, **18**(10), 745-752.
Xu, T., Ma, T.H., Tang, C.A. and Liang, Z.Z. (2006), "Three dimensional numerical approach to splitting failure of rock discs", *Key Eng. Mater.*, 353-358, 921-924.
Yang, J., Ye, J. and Niu, Z. (2008), "Simplified solutions for the stress transfer in concrete beams bonded with FRP plates", *Eng. Struct.*, **30**(2), 533-545.
Yao, J., Teng, J.G. and Chen, J.F. (2005), "Experimental study on FRP-to-concrete bonded joints", *Compos. Part*

B-Eng., **36**(2), 99-113.
Yuan, H., Teng, J.G., Seracino, R., Wu, Z.S. and Yao, J. (2004), "Full-range behavior of FRP-to-concrete bonded joints", *Eng. Struct.*, **26**(5), 553-565.
Zhang, Y. (2007), "The research on parallel compuatation method of rock failure processanalysis", Ph.D, Northeastern University, Shenyang.
Zhang, Y.B., Tang, C.A., Liang, Z.Z., Xu, T. and Li, L.L. (2006), "Research on parallel computational method of rock failure process analysis system", *Chin. J. Rock Mech. Eng.,* **25**(9), 1795-1801.
Zhu, W.C., Teng, J.G. and Tang, C.A. (2004), "Mesomechanical model for concrete. Part I: Model development", *Mag. Concrete Res.,* **56**(6), 313-330.